CONCEPT OF THE VLHC PHOTON STOP EXPERIMENT IN THE APS SYNCHROTRON RADIATION BEAM LINE

P. Bauer, A. Barcikowski*, K. Ewald, C.F. Foerster***, P. Limon, J. Noonan*, R. Rosenberg*, E. Rotela*, B. Rusthoven*, S. Sharma*, M. Pivi**, I. Terechkine, W. C. Turner**

Fermilab, Technical Division
*Argonne National Lab, APS Division
**Lawrence Berkeley Lab, APFR Division
***Brookhaven National Lab, NSLS Division

As part of Fermilab's recent Very Large Hadron Collider (VLHC) feasibility study, a water-cooled photon stop was proposed as a possibility to intercept the intense synchrotron radiation in the high field stage VLHC with minimal plug-power. The photon stop, if feasible, promises not only significant savings in cooling power compared to a solution in which the synchrotron radiation is extracted from a beam screen at cryogenic temperatures, but also virtually removes the synchrotron radiation limitation to beam energy and luminosity in a future VLHC.

A first series of tests is being prepared at the Advanced Photon Source (APS) synchrotron light source at Argonne National Lab. These tests should verify thermal models and yield information about photo-induced gas and electron desorption as well as X-ray fluorescence from the photon stop exposed to synchrotron radiation from bending and undulator magnets. The following presents a concept for the thermal and vacuum-related measurements that should be conducted in the course of these tests.

1) A PHOTON STOP FOR THE VLHC

A very large hadron collider (VLHC) is being proposed as a possible successor to the Large Hadron Collider (LHC). The latest set of general characteristics of the second stage of this machine, as recently studied [1], is listed in Table 1. The second stage VLHC, referred to as VLHC2 in the ongoing text, will produce protons at energies more than 10 times larger than the LHC. Unlike the first stage, the second stage VLHC beams will emit considerable synchrotron radiation power, when steered through the high field magnets.

Energy per proton E_p @ collision(TeV)	87.5
Gamma γ	93284
Peak luminosity L (cm^{-2}s^{-1})	$2 \cdot 10^{34}$
Total circumference C (km)	233
Arc bending radius ρ (km)	29.9
Dipole field B @ collision (T)	9.7
Number of bunches N_b	37152
Initial Nr. of protons per bunch $N_{p/b}$	$7.5 \cdot 10^9$
Initial beam current I_b (mA)	57.4
Bunch spacing t_b (ns)	18.8
Radiation damping time τ_R (hrs)	2.5
Revolution frequency f_0 (Hz)	1286
Normal. (round) beam emittance ε_N @ collis. (rms) (mm-mrad)	$0.08 \cdot \pi$

Table 1: VLHC2 machine parameters (according to [1]).

The synchrotron radiation power radiated by the stage 2 beam, calculated with the parameters of Table 1, is listed in Table 2 together with the other synchrotron radiation characteristics. A more detailed description of the calculations is given in [2],[3]. The synchrotron radiation power in this VLHC2 scenario amounts to ~5 W/m per beam.

Synchrotron radiation power p, per m, per beam (W/m)	4.7
Critical energy E_c (keV)	8.03
Number of incident photons per meter Γ (m^{-1}s^{-1})	$1.2 \cdot 10^{16}$
Incidence angle of synchrotron radiation (mrad)	1.31
Azimuth. (rms) width of synchr. rad. strip on beam-tube/photon-stop*(mm)	0.5
Radial (rms) width of synchr. rad. strip on the photon stop* (mm)	10

Table 2: Synchrotron radiation parameters in the VLHC2. *Calculated for 14 m long magnets and 3 m long magnet inter-connects.

The synchrotron radiation power in the VLHC2, with the operational parameters listed in Table 1, is ~50 times larger than in the case of the LHC. Figure 2 shows the synchrotron radiation power and photon number spectrum emitted by one 14 m long VLHC bending magnet at collision energy. Standard formulae, summarized in [11], were used for the calculation of the graphs shown in Figure 2. The energy spectrum in the plot was arbitrarily cut-off at 0.01 and 4 E_c, accounting for ~95 % of the total radiation power. Half of the power is carried by photons with energies above the critical energy, E_c.

The cost at the plug for removing this synchrotron radiation heat load at low temperature is considerable. A more thorough discussion of cooling issues is given in [4], [5], [6]. According to these calculations the plug power requirement for extracting the synchrotron radiation heat load could be significantly reduced by photon stops operating at room temperature. Photon stops are water-cooled devices that protrude into the beam tube at the end of each bending magnet and scrape off the synchrotron light beam emitted in the second magnet up-stream from their location (see sketch in Figure 1). Radiation fan geometry and cooling requirements demand a certain photon stop surface [7]. The shape of the photon stop mainly responds to stipulations regarding its impedance. A detailed discussion of the impedance related implications of the photon stop and the results of numerical impedance calculations are reported elsewhere [8]. The general implications of photon stops for VLHC's are discussed in [9]. A first photon stop prototype was designed and manufactured. It is shown in Figure 1.
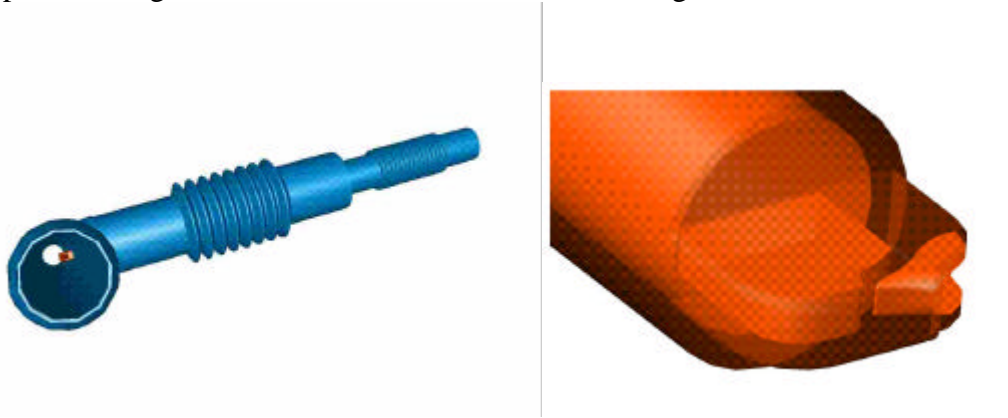

Figure 1: Conceptual design of photon stop: assembly (left), absorber (right). The absorber cavity can be seen on the right side. The larger structure shown in the left part of the absorber piece is a cavity containing the cooling water.

The main issues regarding photon stops are related to operations (and reliability), its effects on the beam (impedance, trapped modes), cryo-design, photo-desorption and vacuum, X-ray fluorescence and e⁻-emission. The high synchrotron radiation flux impinging on the photon stop causes massive gas desorption. It is believed that this effect will allow rapid cleaning (beam-scrubbing) of the device and no vacuum related complications are expected thereafter. X-ray fluorescence and e⁻-emission will be the major remaining "vacuum" issues. The following describes a possible path for the first set of photon stop experiments to be performed at the APS. A rough outline of a possible longer term photon stop R&D plan is given in [10].

The synchrotron radiation experiments proposed in the following aim at matching approximately the characteristics of the synchrotron radiation emitted in the VLHC2 bending magnets.
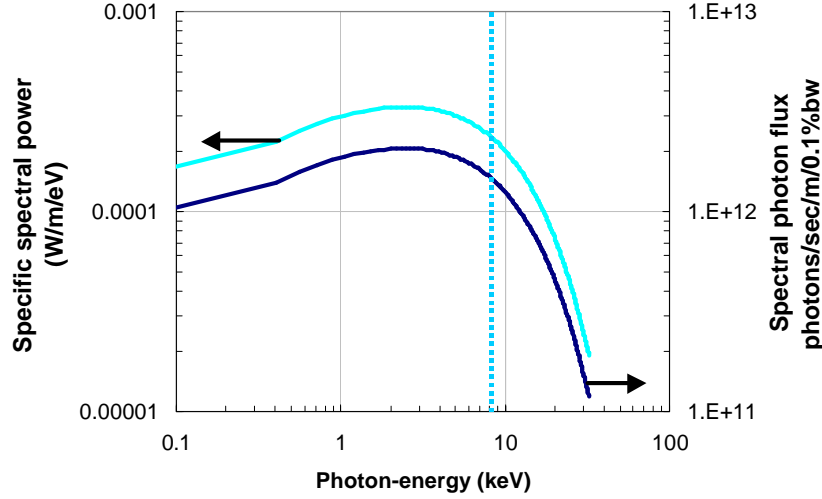
Figure 2: Spectral synchrotron radiation power and photon number distribution of synchrotron radiation photon flux (1 beam) per m of VLHC2 dipole. The VLHC2 high field dipoles are ~14 m long. The vertical dashed line indicates the critical energy of the synchrotron radiation spectrum.

2) MEASURING AT THE ADVANCED PHOTON SOURCE

The Advanced Photon Source (APS) at Argonne National Laboratory is a national synchrotron-radiation light source research facility. The APS is funded by the U.S. Department of Energy, Office of Basic Energy Sciences. The synchrotron light is produced by 60 bunches a $3.6 \cdot 10^{10}$ electrons, giving an average 100 mA e$^-$-beam, with a particle energy of 7 GeV (g=13844). There are two distinct sources of synchrotron radiation around the ring:

- 0.6 T bending magnets with a 19 keV critical energy;
- 0.84 T peak field undulator magnets (type A), which can be tuned to produce a first harmonic peak in the range 3-14 keV photon energy;

The accelerator physics group at APS has extensive experience in the design of synchrotron radiation absorbers, commonly used in the APS ring. The APD/APS maintains a special beam-line ("diagnostics" beam-line, see Figure 4) that could be available for photon stop testing. The diagnostics beam-line undulator characteristics are:

- 0.274 T peak field, ~25 keV (or higher) first harmonic peak;

The total synchrotron radiation power emitted per bending magnet is 6.83 kW, at a flux of $1.6 \cdot 10^{13}$ photons/sec/mrad. The bending magnet power is given for the total fan width of 78 mrad – only 7 mrad are extracted toward the experimental sections. The photon stop will be placed at approximately 25 m from the radiation source. The radiation absorbing cavity at the tip of the stop is ~5 mm wide, such that only the central 0.2 mrad of the radiation beam will hit the absorber cavity. Therefore only the 0.2/78th part of the 6.83 kW from the bending magnet will be useful, resulting in 17.5 W of power. In a VLHC setting the photon stop would have to absorb ~100 W of radiation power (see
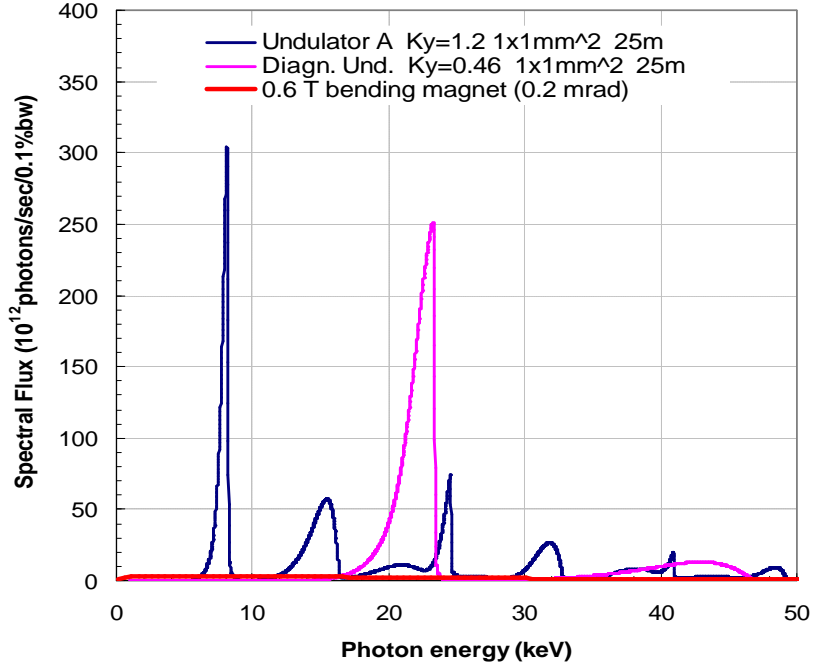
Figure 3: Spectral flux distribution for APS undulators (A and diagnostics) after $1 \times 1mm^2$ collimation (settings as in Table 3). Shown as well is the continuous spectrum of the 0.6 T APS bending magnet radiation after horizontal collimation to 0.2 mrad. The bending radiation level is too small to be seen here (see Figure 14 for a better picture). Calculations performed with XOP;

Table 2). To attain this power the undulator beam, which can yield larger power and flux is required. An additional advantage of the undulator beam is that its radiation is almost monochromatic. Figure 3 shows the calculated photon flux spectra for the APS undulators and bending magnets. To limit the total radiation power of the undulator beams to ~ 100W, a 1 mm x 1 mm collimation is assumed. The flux spectrum, integrated flux and power were calculated with XOP (courtesy of ESRF, Grenoble). A compilation of practical formulas describing undulator and bending magnet radiation is given in [11]. Table 3 lists the undulator parameters used in the calculations. The undulator gap was chosen to be such that the first harmonic matches as closely as possible 8 keV, the VLHC2 synchrotron radiation critical energy.

Parameter	Undulator A	Diagnostics
Undulator gap (mm) – (chosen)	18	10.5
Undulator period (cm)	3.3	1.8
Number of periods	72	198
Effective field (T) / Deflection parameter K_y	0.387 / 1.2	0.274 / 0.46
Energy ($1^{st}/3^{rd}/5^{th}$ harmonic) (keV)	8.24 / 24.7 / 51.2	23.4 / 70.2 / 117
Total power emitted by undulator (kW)	1.1	0.83
Total power after $1 \times 1 \ mm^2$ collimation (W)	89	104.4
Total flux after $1 \times 1 \ mm^2$ collimation (10^{16}/sec)	4.08	2.76

Table 3: Nominal parameters of APS undulators for the photon stop experiment. Power calculated at 25 m from the source with XOP, including all harmonics up to n=33.
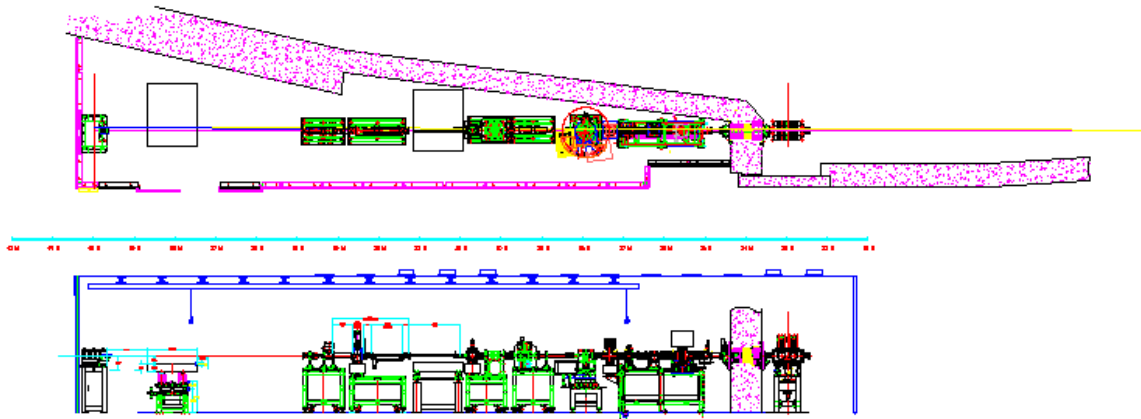
Figure 4: APS diagnostics beam-line layout. The light beam enters from the right.

3) PHOTON STOP PROTOTYPE DESIGN

A photon stop prototype was designed for the purpose of testing in the diagnostics beam-line at the APS. A sketch of the design is shown in Figure 5. The design is currently being upgraded to include a step-motor drive system for remotely controlled in and out motion. The accelerator technology group at the APS has recently completed a similar device that will be used as the basis for the design of the photon stop test hardware. Figure 5 shows how the photon stop mounts into a 4-way cross, with the beam entering (exiting) through the horizontal ports and a lower vertical port for an ionization pump.
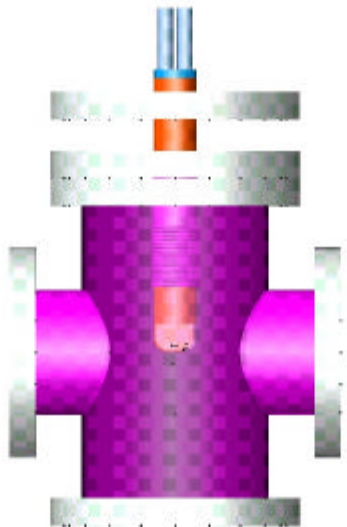

Figure 5: First pass design of photon stop experiment set-up.

4) PHOTON STOP EXPERIMENTAL MODEL

4.1) Photo Induced Desorption - Vacuum

A large number of vacuum measurements were conducted in the context of the SSC and LHC machine development, generating a vast amount of photo-desorption data for various materials, surface preparations, temperatures, radiation incidence angles and characteristic radiation energies (see for example references [12] and [13]). A summary of the experimental SSC/LHC photo-desorption data of interest for the photon-stop experiment is given in [14]. As discussed in [14] the photo-desorption of strongly bound surface gases from a copper surface can be described with the following fit, (1),

$$h = h_0 \left(\frac{\Gamma'}{\Gamma'_0} \right)^{-n} \quad \left(\frac{molecules}{photon} \right), \tag{1}$$

where h_0 (molecules/photon) is the desorption coefficient at the reference surface photon flux G'_0 (photons/m^2), G' (photons/m^2) is the integrated surface photon flux and n the slope parameter. The parameters of (1) for the desorption of the most common UHV gases from a "technical" copper surface are listed in Table 4. A plot showing the so found desorption coefficients as a function of photon dose is shown in Figure 7.

Table 4: Numerical values and parameters used for the vacuum model [as summarized in 14]. The transition photon dose Γ_0' is assumed to be $4 \cdot 10^{19}$ photons/m^2. The thermal desorption $Q_{j,tds}$ are for in-situ baked, clean surfaces after 50 hrs of pumping [as summarized in 14].* H_2O desorption data are from the Cern/EPA experiment [se as well summary in 14].

gas j	η_{0j} (molec/phot) –Copper surface – normal incidence	v_j	$Q_{j,tds}$ (nTorr-liter/s-m^2)	f_j
H_2	0.0036	0.45	10	3.74
CO	0.00077	0.48	0.1	1
H_2O*	0.00065	0.35	0.1	1.25
CO_2	0.00031	0.45	0.05	0.8
CH_4	0.00006	0.48	0.05	1.32

The pressure rise in the test volume V (liter) due to photon induced desorption from the photon stop surface A_{PS} (m^2) can be calculated with (2), where G' is the time integrated surface flux (photons/m^2) and h_{SR} is the photo-desorption coefficient (molecules per photon), depending on G'. The "active" photon stop surface, A_{PS}, that is the surface of the bounding walls of the absorbing cavity (Figure 6) hit by the primary radiation beam, is 278.7 mm^2 .

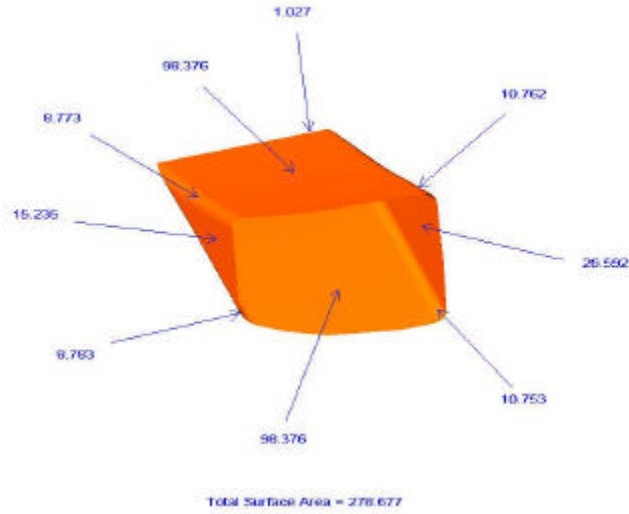$$\Delta p(t) = 3 \cdot 10^{-11} h_{SR} \left(\Gamma'(t) \right) \Gamma'(t) A_{PS} \frac{1}{V} \quad (nTorr) \tag{2}$$

Figure 6: Photon stop absorber cavity (surfaces in mm^2). The cavity opening angle ("linearized") is 22.5°. The cavity entrance window area is 6x8 mm^2 ("flat").

The proportionality factor in (2) converts the number of desorbed molecules to nTorr-liter:

$$Const = \frac{294K}{273K} \frac{760\frac{Torr}{atm} \, 22.4\frac{liter}{mol}}{6.02 \cdot 10^{23} \frac{molecules}{mol}} \cdot 10^9 = 3.05 \cdot 10^{-11} \frac{nTorr - liter}{\# \, of \, molecules}$$
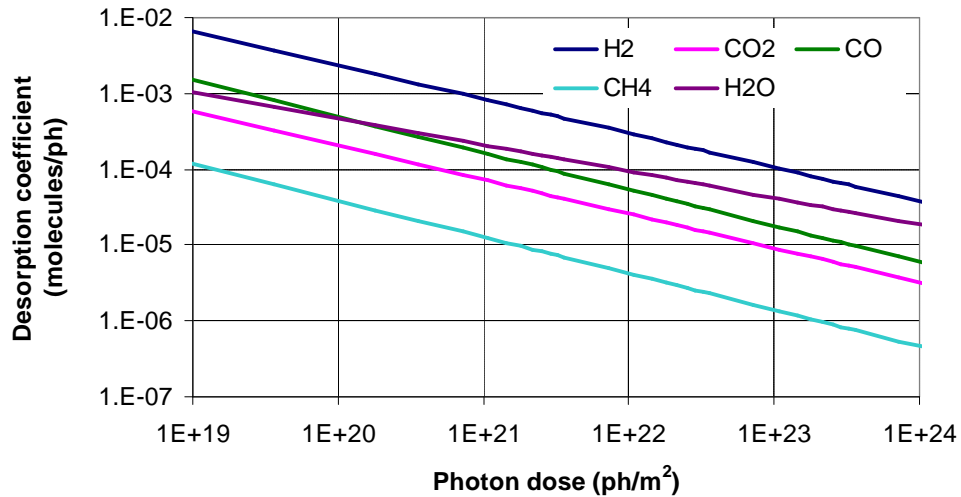

Figure 7: Photo-desorption of H_2, CO, CO_2, H_2O and CH_4 at a photon flux $=10^{17}$ photons/sec from a 240 mm^2 photon stop surface as a function of integrated photon dose. Desorption coefficients from Table 4. Reference (integrated) flux $\Gamma_0'=4\cdot 10^{19}$ photons/m^2.

8

The total pressure in the test volume as a result of photo-desorption of H_2, CO, CO_2, H_2O and CH_4 from the photon stop surface (see Figure 8), is therefore given as $p_0 + \boldsymbol{D}p(t)$, where p_0 is the baseline pressure of the experiment (assumed to be 0.1 nTorr). This calculation obviously neglects the "background", that is the photo-desorption from the vacuum chamber surfaces enclosing the photon stop, as well as thermal desorption.
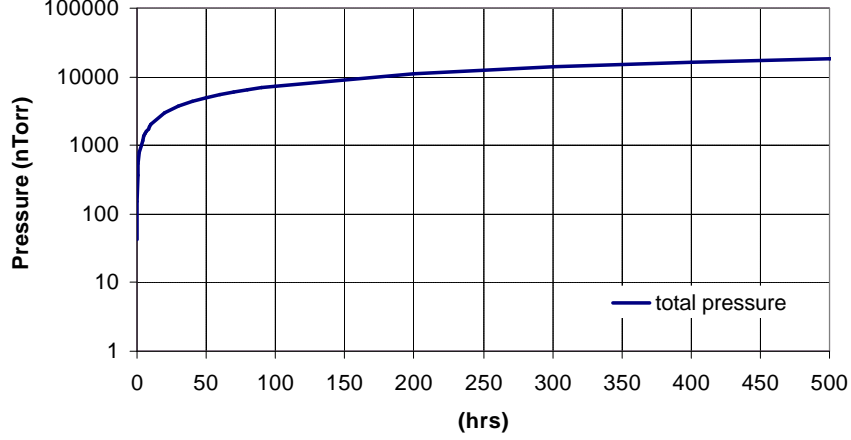

Figure 8: Pressure rise in 10 liter test volume as a result of photo-desorption of H_2, CO, CO_2, H_2O and CH_4 , photon flux $=10^{17}$ photons/sec, from a 240 mm^2 photon stop surface. Initial pressure = 0.1 nTorr; Desorption coefficients from Table 4.

In a real accelerator setting the pressure cannot be allowed to rise (such as in Figure 8) and therefore an adequate level of pumping has to be provided. Preliminary calculations, [15], have shown that a ~100 lit/sec cryo-pump is sufficient (e.g. 1m of a perforated high temperature liner inside a cryogenic tube). The equilibrium pressure in the test volume V can be calculated as a function of the pumping speed S (liter/sec) with the following set of equations. The photo-desorption rate is:

$$Q_{j,photo} = 3 \cdot 10^{-11} \boldsymbol{h}_{SRj}(\Gamma')\dot{\Gamma}' A_{PS} \left(\frac{nTorr - lit}{\sec} \right) \tag{3}$$

The partial pressure p_j of gas j for a pumping speed S_j (liter/sec) can be calculated with:

$$p_j = \frac{\left(Q_{j,photo} + Q_{j,therm} \right)}{S_j} \quad (nTorr) \tag{4}$$

where $Q_{j,photo}$ is the photo-desorption rate of gas j, (3), and $Q_{j,therm}$, the thermal desorption rate as given in Table 4. The f-factor (Table 4) can be used to express the pumping speed for all gases relative to the pumping speed for CO. This factor depends on the pumping method – the numbers indicated in the table being representative of a cryo-pump, where the difference in pumping speed for different gases is determined by the difference of the molecular speeds. For this particular calculation the integrated photon flux has to be fixed in (3) – here it was fixed to 0.1 hrs of operation at 10^{17} photons/sec/m^2, typical for the
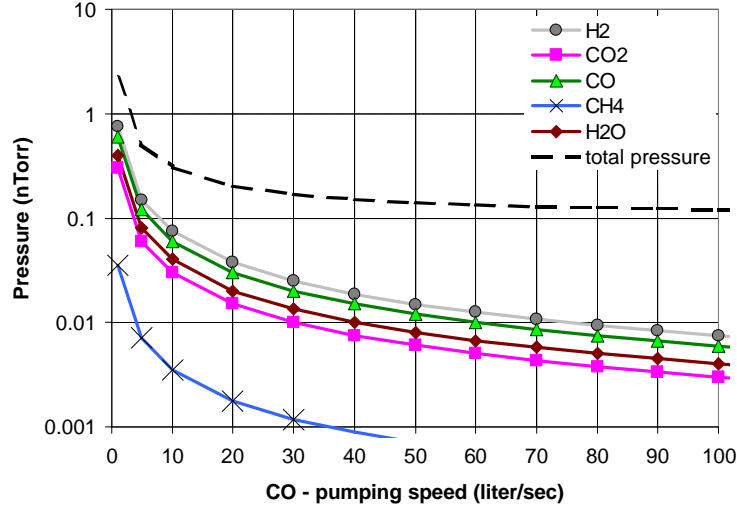
Figure 9: Pressure change in 10 liter test volume as a result of photo-desorption and thermal desorption of H_2, CO, CO_2, H_2O and CH_4, photon flux = 10^{17} photons/sec, from a 240 mm^2 photon stop surface after a 0.1 hrs irradiation as function of pumping speed (CO-equivalent). Background pressure = 0.1 nTorr; Desorption coefficients from Table 4.
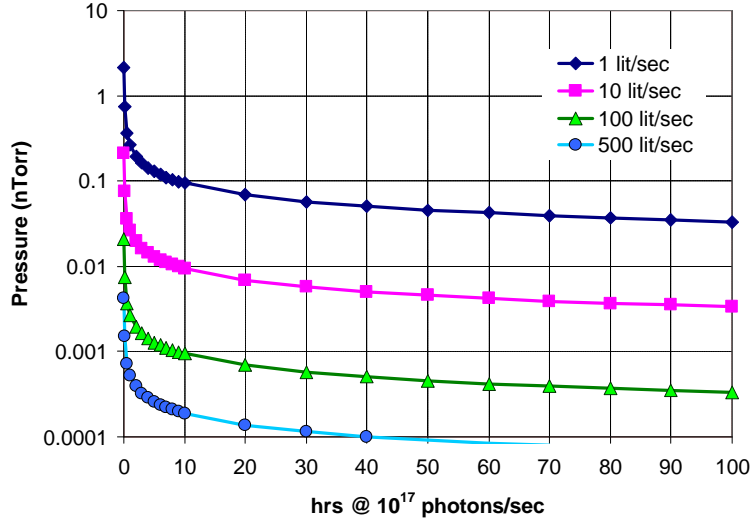

Figure 10: Pressure change in 10 liter test volume as a result of photo-desorption and thermal desorption of H_2 for different CO-equivalent pumping speeds as a function of irradiation time. Photon flux = 10^{17} photons/sec, desorption from a 240 mm^2 photon stop surface; No thermal desorption included. Desorption coefficients from Table 4.

APS undulators (see Table 3). The total pressure is obtained from the sum of the partial pressures p_j of the "usual" UHV gases listed in Table 4 (and the background pressure p_0). Figure 9 and Figure 10 show two variants of a possible measurement of the effect of pumping speed on the final pressure in the test-volume. First, the pressure after 0.1 hrs of irradiation due to photo-induced and thermal desorption is evaluated for each gas species as a function of pumping speed (Figure 9). In Figure 10 the H_2 partial pressure is shown as a function of irradiation time for a fixed pumping speed. Figure 9 and Figure 10 show

that a) the pressure signals in the photon stop photo-desorption tests will be minute and b) the photo-induced desorption will not be the major concern regarding photon stops in accelerators (unless radiation misses the absorber).

4.2) Photo Induced Electron Emission

An estimate of the photo-desorbed charge can be obtained on the basis of:

$$Q_{el} = \boldsymbol{h}_e(\Gamma')\dot{\Gamma}'A_{PS}e \quad \left(\frac{C}{\sec}\right), \tag{5}$$

where $\boldsymbol{h}_e$, according to the CERN/DCI experiments (see summary in [14]) is given by

$$\boldsymbol{h}_e(\Gamma') = 1.25 \cdot 10^{-46}\Gamma'^2 - 7.5 \cdot 10^{-24}\Gamma' + 0.25 \quad \left(\frac{electrons}{photon}\right) \tag{6}$$

as a function of the integrated surface flux $\boldsymbol{G}'$ (photons/m^2). A plot of Q_{el} is given in Figure 11.
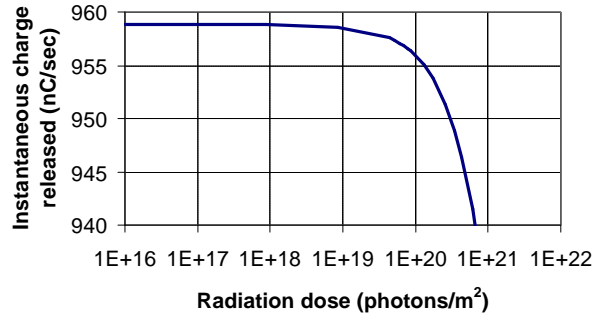

Figure 11: Charge released due to photo-induced desorption as a function of integrated radiation dose. Flux = 10^{17} photons/sec, from a 240 mm^2 photon stop surface, e$^-$ desorption coefficient as in (6).

The emitted photo-electron spectrum is well known for VUV as well as selected keV energies, but not very well documented for 10 keV incident photon energies and higher. An example of a photo-emission spectrum is given in Figure 12. The spectrum peaks at a few eV and drops quickly toward higher energy.
It is believed that biasing of the photon stop with a ~100 V voltage should be sufficient to suppress most of the electron emission. This measure requires that the photon stop is isolated from ground.
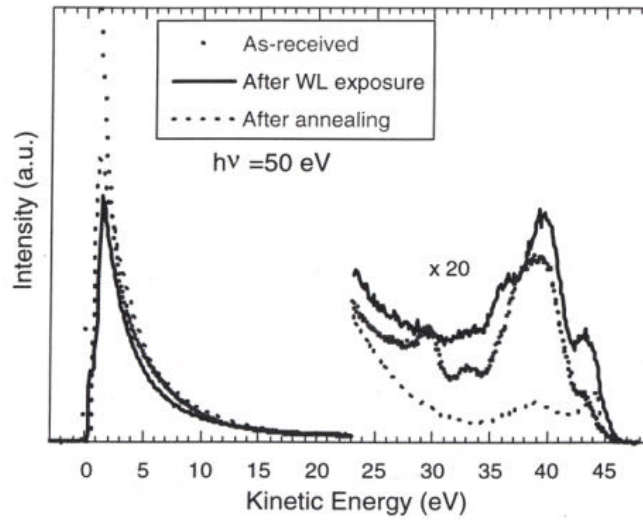
Figure 6: Photoemission spectra of Cu-el. taken at 50 eV photon energy of: a) as-received; b) after WL exposure; c) after annealing in UHV (pressure during annealing was less than 5 10⁹ mbar) at 300 ± 50 °C for 2.25 hours (Cu-el.-an.).

Figure 12: Photoelectron emission spectrum for Cu reported in [16].

4.3) Scattering, Reflection and X-ray Fluorescence

The wedge-design of the photon stop cavity together with the "natural" surface roughness should allow trapping of most of the entering photons. Reflection, especially at higher photon energy is only occurring at grazing incidence. It is unlikely that photons will be scattered back out of the cavity, since that would require multiple incidence at grazing (mrad) angles. Therefore, in first approximation, the model discussed here assumes that the only photons leaving the photon stop are emitted through X-ray fluorescence. The fluorescence K and L line spectrum for some selected materials is indicated in Table 5, where, usually, only $K\alpha 1$ has a significant yield (see Table 6). The photon attenuation lengths are listed as well (see Table 7), because of their relevance to the issue of photons penetrating through the bounding walls of the photon stop cavity and the issue of coating thickness. The attenuation lengths are sufficiently small to assume that the photon flux

Table 5: X-ray emission lines in keV. Data from [17].

Material	$K\alpha 1$	$K\alpha 2$	$K\beta 1$	$L\alpha 1$	$L\alpha 2$	$L\beta 1$
Copper	8.048	8.028	8.905	0.930	0.930	0.950
Silver	22.163	21.990	24.942	2.984	2.978	3.151

Table 6: X-ray fluorescence yield for K and L lines (average). Data from [18].

Material	K1	L1	L2	L1
Copper	0.44	0.0016	0.01	0.01
Silver	0.831	0.016	0.051	0.052

Table 7: X-ray attenuation lengths at different energies (keV) for copper and silver. Data calculated from the mass attenuation coefficients listed in [19], with 8.02 g/cm^3 for the density of copper and 9.32 g/cm^3 for the density of silver.

Material	1 keV	10 keV	100 keV	500 keV
Copper	0.12 µm	5.8 µm	2.7 mm	1.48 cm
Silver	1.5 µm	9.02 µm	0.73 mm	1.15 cm

emitted into any angle except the solid angle element covering the cavity entrance window will be absorbed in the material. It can furthermore be concluded that a 1 mm coating thickness is required for potential coating candidates, if the underlying material (that is copper) is to be shielded from the primary radiation. This considerable coating thickness sets a constraint on the coating technologies that can be used. The fluorescence flux emitted by the absorber was calculated using equation (7) following a procedure presented in [20]. Equation 7 describes the fluorescence flux collected into a detector surface area *A* at a distance *r* from the emitting site as a result of primary irradiation with a flux of spectrum dG_{in}/dE. The most important part of (7) is the energy-dependent, integrated absorption coefficient, which was calculated from a model including the effect of "self-absorption" (that is the effect of absorption of not only the primary photons but also the absorption of the generated fluorescence radiation on its way out of the sample). Consider a flat sample with thickness *d*. Photons of energy *E* enter the sample at an angle ***a*** to the plane of incidence. The incoming radiation is absorbed according to the total absorption coefficient (or cross-section) ***m***$_{ot}$. If *E* is sufficiently high, the photon produces a core hole, which then can, with the fluorescence yield probability w_x, decay to produce a fluorescent photon of energy E_{fl}. The produced fluorescent radiation is absorbed according to ***m***$_{ot}(E_{fl})$. The probability of a photon leaving the sample at a take-off angle ***b*** can be found by integrating the law of absorption over the paths of the photons through the sample. The variation of ***b*** due to the solid angle A/r^2 covered by the detector is assumed to be small. Furthermore the sample is assumed to be much thicker than the photon penetration depth (see Table 7).

$$\frac{d\dot{\Gamma}_{fl}}{dE} \approx \frac{d\dot{\Gamma}_{in}}{dE}\frac{A}{r^2}w_x\frac{m_{tot}(E)}{m_{tot}(E)+m_{tot}(E_{fl})\frac{\sin a}{\sin b}} \quad \left(\frac{fl\ photons}{sec-keV}\right) \tag{7}$$

The cross-sections, used in the calculations, for some materials of interest are shown in Figure 13. Note that for the calculation in (7) the cross-section is artificially set to zero below the X-ray absorption edge of interest.

A computation of the fluorescence yield from the absorber cavity for an incoming photon spectrum of the APS bending magnet and the APS undulator A type is shown in the following figures. Figure 14 shows the out-coming flux of Kα1 fluorescence in copper and Figure 15 the fluorescence flux from the Kα1 and Lα1 lines (against the background of the incoming flux spectrum). The K and L line fluorescence in Ag were computed independently. The incidence and emission angles ***a,b*** are assumed to be π/2 in this case (vertical incidence and emission). The solid angle element A/r^2 covered was assumed to
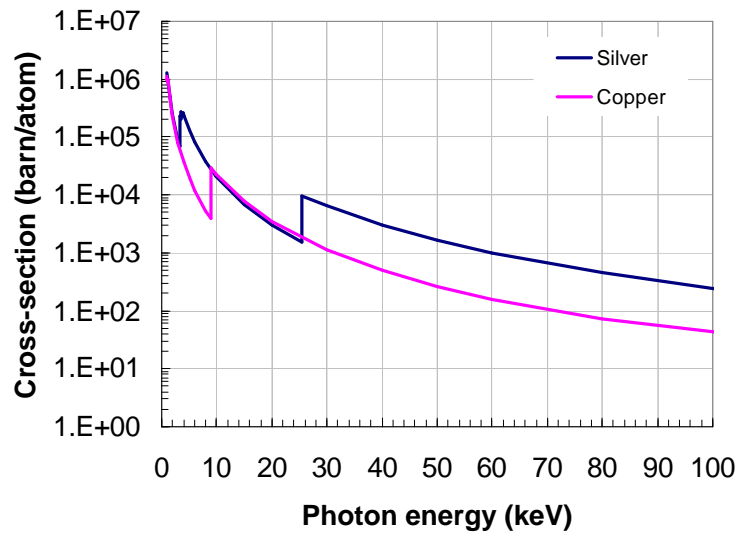
Figure 13: Photo cross-section for different materials, computed with XCOM.
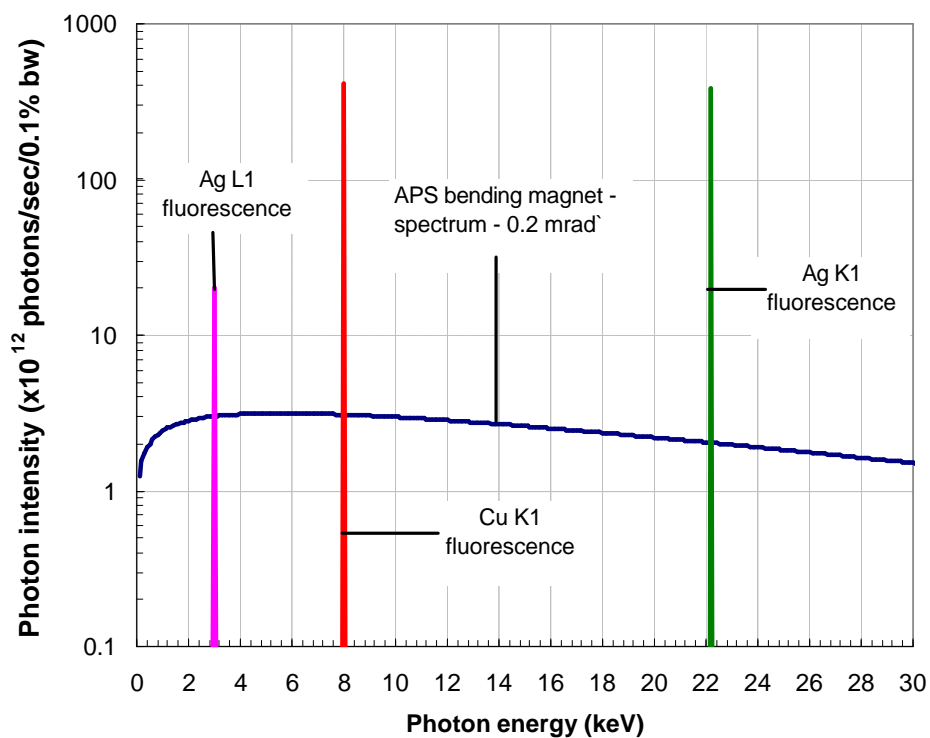

Figure 14: The calculated fluorescence of photon stop in APS bending magnet (1 m) radiation beam for copper and silver. Note that the fluorescence flux represents the integrated number of photons per second at the respective X-ray edge energy.

14

Figure 15: The calculated fluorescence of a copper or silver photon stop in APS undulator. Note that the fluorescence flux represents the integrated number of photons per second at the respective X-ray edge energy.

Figure 16: The calculated fluorescence of a copper or silver photon stop in a VLHC2 bending magnet (14 m length) radiation. Note that the fluorescence flux represents the integrated number of photons per second at the respective X-ray edge energy.

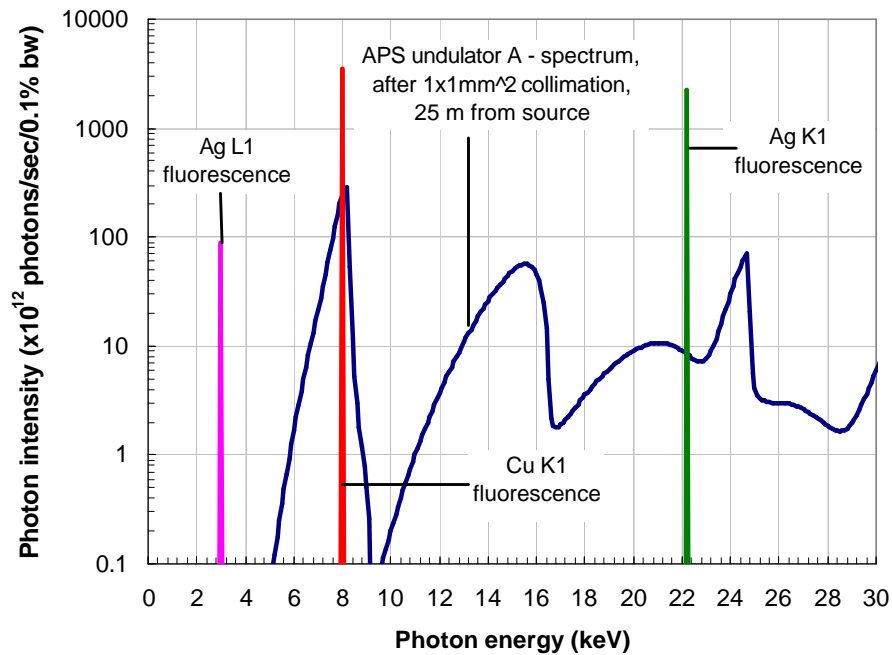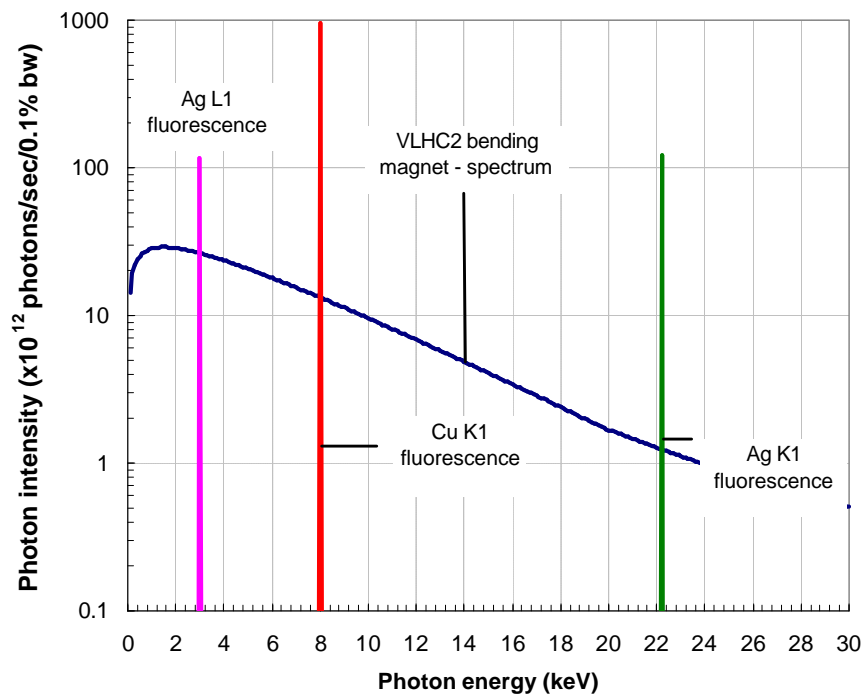be the total cavity window size ($6\times8mm^2/1cm^2$). The line characteristics and their fluorescence probabilities used in the calculations are listed in Table 5 and Table 6. The calculation results, shown in Figure 14 - Figure 16, reveal that, a considerable fluorescence flux escapes from the photon stop. This flux, together with the power carried by the fluorescent photons, is indicated in Table 8 for the case of the VLHC2 bending radiation. As can be derived from a comparison with the VLHC2 synchrotron radiation power per beam, ~2% of the power escapes via fluorescence. A silver coating, as can be concluded from Table 8, would allow a three-fold reduction in fluorescence flux. The silver coating has the advantage that it provides good thermal conductivity and that the coating can be made thick (through electro-plating). A more thorough analysis of possible coating candidates has not been performed. Among other possible coatings that could be pursued, SiC seems promising.

Table 8: Calculated X-ray fluorescence yield from a VLHC2 photon stop (see Figure 16) – photon flux and power.

Material	$\Gamma(10^{14}$ photons/sec)	p (W)
Cu K1	9.63	1.23
Ag K1	1.22	0.43
Ag L1	1.17	0.06

4.4) Thermal Performance Simulation

Assuming that a single photon-stop intercepts the synchrotron radiation heat load emanating from one 14 m long VLHC2 bending magnet, its thermal load is ~70 W. The results of a thermal performance simulation of the room temperature part of the photon stop insert have been reported in [7]. The main results are summarized in Table 9. Water was chosen as the refrigeration liquid. The peak heat flux is below the critical surface heat flux of water ($2~MW/m^2$). Other coolants, with lower freezing temperatures, should be investigated.

Table 9: Results and parameters of the photon stop thermal model.

Photon-stop Cooling System Parameters	
Synchrotron heat load per device (W)	70
Surface heat exchange area (cm^2)	1
Wall thickness heat exchanger (mm)	1
Heat exchanger surface temperature – beam side (K)	360
Heat exchanger surface temperature – coolant side (K)	305
Peak heat flux into coolant (MW/m^2)	0.6
Coolant flow rate (liters/s)	0.2
Coolant velocity (m/s)	2.6
Coolant inlet temperature (K)	300
Coolant outlet temperature (K)	305
Cooling tube inner diameter (mm)	10

4.5) Model Summary

The model calculations presented above can be summarized with the following:

- "Beam-scrubbing", that is the reduction of photo-desorption coefficient with time is fast due to the small surface involved (typical VLHC2 flux ~ $6 \cdot 10^{20}$ ph/sec/m^2), thus reducing measurement times considerably. The measurement of the desorption coefficient – for example via (4) – will require a sub-nTorr pressure resolution (see Figure 10), which will be difficult to achieve. It is believed that after fast conditioning the photon stop will not represent any further vacuum issues in a VLHC2.
- the electron yield current should be typically of the order of some µA, which can be measured with standard wire-electrodes. A 100 V bias should suppress most of the electron emission activity from the photon-stop.
- The fluorescence yield from the photon stop cavity was calculated, showing that a few percent of the incoming power will be emitted back out of the absorber via X-ray fluorescence. Fluorescence can only be reduced using particular coatings and therefore different coatings should be investigated.

There are however serious issues that have not been addressed in the model. Some of them will be discussed in more detail in part 5). The most important is the large background in the vacuum measurement: the surface surrounding the photon stop is 100-1000 times larger than the surface of primary radiation incidence within the absorber cavity. Photons, reflected or scattered from the PS will most likely desorb many more gas molecules than emitted by the area of primary beam incidence. Former, similar, measurements have suffered from this problem [21].

5) PROPOSED PHOTON STOP TEST AT THE APS

5.1) Objectives of the Test

The following test objectives are of interest:

- Desorption coefficient per gas species as a function of radiation dose, photon energy and beam power;
- Electron yield estimate;
- Fluorescence flux estimate;
- Measurement of the thermal performance of the photon stop, i.e. measurement of tip temperature as a function of cooling water flow;

With a flux of ~10^{16} ph/sec or more (such as in the undulator beam), corresponding to a surface flux of $4 \cdot 10^{19}$ ph/m^2 on the photon stop, integrated doses of 10^{24} ph/m^2 can be accumulated in 15 hrs. If the white light from a bending magnet is used ($\overset{.}{G}$~10^{12} photons/sec), the measurement time (even for a reduced objective of say 10^{22} ph/m^2) can become considerably longer (if not too long). Beyond integrated fluxes of 10^{24} ph/m^2 the surfaces are well cleaned, such that we expect no need to extend the measurements

beyond this range. The base-line pressure in the system should be 0.1 nTorr. Since this is typical for the APS beam-line, the standard APS cleaning procedures should be sufficient (degreasing with Citronox, 150° C, 48 hrs in situ bake). The pre-measurement bake-out will be more time consuming than the measurements. RGA calibration has to be included as well in the measurement preparation procedure. To reduce background some parts (e.g. the funnel) could be baked at high temperatures (e.g. 1 hr at 900° C). The photon stop should be prepared in a way that is representative of the "accelerator" case. The following systems must be part of the experiment (most are available at ANL):

- Leak valve for calibration of the RGA;
- Safety shutter, beam stop, fast valve + instrumentation, controls and feed-back;
- Collimator system (remote controlled ?) to be varied in the range 0.1 – 2 mm vertically and 0.2 – 4 mm horizontally;
- Water cooled iris (central hole radius ~ 0.3 mm)
- Two 200 lit/sec ion pumps + one 30 lit/sec ion pump + one TMP;
- Regulated water valve in the range 0.1-0.5 lit/sec (e.g. Yokogawa 6 gpm);
- Minimum of 2 BA's and one RGA;
- Temperature sensor, e.g. thermo-couple;
- IR-temperature measurement system;
- A ~ 2" gate valve to gate off the TMP;
- 100 V, battery based voltage bias for photon stop and funnel;

5.2) Sketch of Measurement System

A photon stop prototype, compatible with the experimental access-port ("cross") for photon stop testing in the APS-APD diagnostics beam-line, was designed and produced. In order to fit into the cross, the photon stop was made shorter (total length ~5 inches) than required in an accelerator magnet setting. If the option of multiple samples (e.g. to test different coatings) on one holder is to be implemented a new absorber will most likely have to be built. A sketch of the cross is shown in Figure 5 and Figure 17. The cross allows access from top (photon stop) and bottom (pump) and connects through the horizontal flanges to the synchrotron radiation beam line. In addition there are two more horizontal access ports (at 60 degrees from the beam line), one for an infra-red window for temperature measurement and the second for additional instrumentation (such as for example a BA gauge).

5.2.1) Thermal test
The thermal performance test of the photon stop will be made using infrared (IR) imaging. In addition a thermocouple mounted in the return water duct would allow monitoring of the temperature rise in the cooling water. A thermo-couple is mounted on the photon stop tip, for the calibration of the IR-camera temperature measurement. The camera is placed in a lead shielded alcove at some distance from the experiment, while the infrared light is brought via mirrors to the lens. The thermo-couples, infrared sensor, flow-regulators and temperature sensors in the cooling water pipes serve to evaluate the

main thermal parameters of the photon stop, i.e. the absorber surface temperature, coolant temperature, flow-rate, etc.

5.2.2) Photo-desorption Measurement
In addition, we propose to perform a vacuum measurement using the procedure sketched in Figure 17 and Figure 26. The photon stop is mounted into the top opening of the test-cross. The (remotely controlled) in-and-out motion is provided by a step-motor. The mechanical structure allowing to move the photon stop up and down has been designed at the APS for the purpose of testing other absorbers. We would like to use a similar system, except for a larger stroke to allow for multiple probes and a ceramic breaker (discussed further in the following).

The main addition that we propose, as shown in Figure 17 and Figure 23, consists of a funnel (or "trumpet"), that allows to direct the desorbed gas molecules toward a small aperture (S1 in Figure 26) into a neighboring, larger adjacent volume (spool). The radiation beam passes as well through this aperture. If needed, the funnel can be cooled with a cooling water spiral surrounding it. It can as well be negatively biased to ground to prevent photo-electrons from being emitted. The adjacent volume, the so-called measurement volume, contains ports for an RGA and a BA-gage and pumping ports, a second volume upstream, the so called pumping volume, contains a strong ion pump (~200 liter/sec). The pump aspires the desorbed gases through the aperture S_1 into the measurement volume, where the pressure measurement instrumentation is placed, and
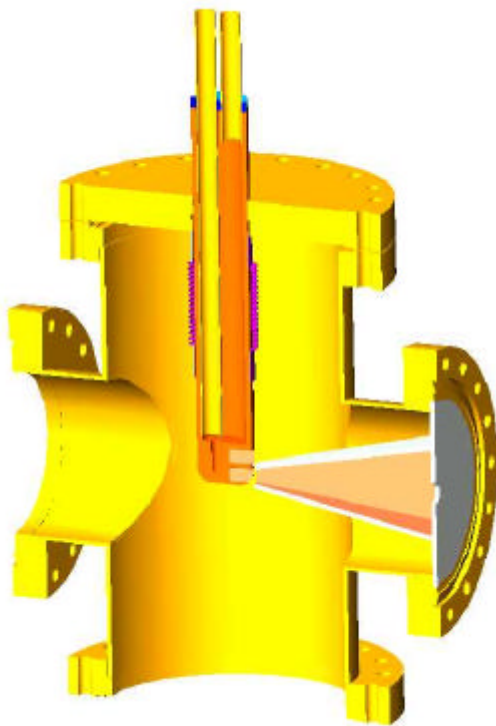

Figure 17: Sketch of photon stop mounted in the APS cross.

then further through S_2 into the pumping volume. The measurement of the pressure in the measurement chamber allows, via the known conductance of the small aperture S_1, to determine indirectly the pressure in the funnel cone containing the desorbed gas-load. The advantage of this approach, so it is hoped, is that the reflected and scattered photons mostly remain within the volume delimited by the funnel. Therefore the probability of photons entering the BA-gage or RGA is low. In addition it reduces the background pressure due to "parasitic" gas desorption, which is the major issue of the vacuum test. As an ultimate measure a tube can be placed into the center of the measurement volume, guiding the light beam to the funnel entrance. The funnel serves mostly one purpose: to reduce the surface area that can contribute to the background desorption and, being a separately mounted piece, allowing it to be prepared to a level of cleanliness that cannot easily be achieved for the complete cross-assembly. In addition, it shields the cross-ion pump from the radiation, which thus does not need to be gated, which saves money. The funnel interferes with the infrared measurement. The IR measurement system will be placed into one of the 60° side-ports, such that it looks at the side-faces of the cavity, which presumably will be at almost the same temperature as the inside. It has to be noted that the IR signal will be calibrated with a thermocouple, affixed to exactly this side surface.

In a low pressure, molecular flow regime the following equation for the gas flux between volumes at pressures p_i connected by a conductance S_j holds (see Figure 26):

$$p_1 S_1 = p_2 S_2 = p_3 S_3 \quad \left(\frac{Torr - liter}{\sec} \right) \qquad (8)$$

The pressure in the funnel p_1 and the (measured) pressure in the adjacent measurement volume p_2 therefore is:

$$p_1 = \frac{S_2}{S_1} p_2 \qquad (9)$$

The ratio of pumping speeds S_2/S_1 is known, because S_2 (pumping speed in adjacent volume) is determined by the conductance of the aperture connecting the measurement volume to the pumping volume and S_1 is equally determined by the size of the connecting aperture. Besides S_2 can be measured by leaking gas into the volume and measuring the pressure decay time. The equipment for leaking gas into the system should be available because it is needed for the RGA calibration procedure. An estimate of the range of aperture radii r required to obtain a reasonable sensitivity can be obtained from the standard formula for the aperture conductance of a circular hole (assuming a transmission probability of 1):

$$S_1 \approx 10^3 \frac{\langle v \rangle}{4} \boldsymbol{p} r^2 \quad \left(\frac{liter}{\sec} \right) \qquad (10)$$

With a molecular speed of ~500 m/s (as for N_2 at room temperature) and a minimum aperture radius of ~1 cm the conductance of the iris is ~40 liter/sec (the flange OD is

~6"). To obtain a p_2/p_1 ratio of 0.1, S_2 has to be ~$S_1/10$, i.e. 4 liter/sec (which corresponds to an orifice radius of 0.3 cm). The p_2/p_1 ratio of 0.1 indicates that 10 nTorr signals in the funnel volume will be translated to nTorr signals in the measurement volume. This is the minimum signal needed for a measurement.

If the iris is a ring-shaped slot at the outer edge of the disc separating the funnel volume from the measurement volume (see Figure 26), the aperture can be made larger without paying the price of increased photon back-scattering into the measurement volume. In addition, the gas molecules that pass the annular gap are more likely to be thermalized because they have to be close to the funnel wall. The irises will not be cooled, provided that an iris similar to S2, with active cooling, is placed up-stream, behind the collimator.
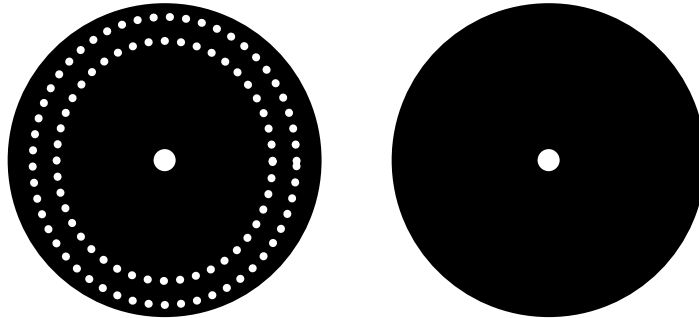

Figure 18: Possible shapes of iris S1 (left) and S2 (right)

The APS has existing designs for such cooled irises. Molecules that shoot straight back against the light beam will be stopped by the disc (which of course needs a small residual opening of some mm^2 for passage of the light beam).

As can be seen in the simulation shown in Figure 10, pumping speeds of 10 liter/sec and more result in very small (sub-nTorr) pressure signals (as a result of the small desorption surface). We believe that, given a base-line of 0.1 nTorr, the expected signals should be at least of this order, requiring pumping speeds below 1 liter/sec through S2, which might require even smaller iris apertures than indicated above. Other issues, such as bake-out and RGA calibration result as well in constraints on the iris size. A large iris radius would be required for efficient bake-out and rough-pumping. Therefore the TMP pump in Figure 26 is connected to both the cross and measurement volume. Note that the TMP has to be gated off (with an all-metal valve). During RGA calibration it might be useful to close the iris completely, or at least make it small.

An important element in dealing with the problematic issue of background is the use of a so called reflector. In the simplest case the reflector is part of the photon-stop, i.e. the area above the absorber cavity. This solution offers the big advantage of not having to supply a separate cooling and motion systems. The radiation beam is directed first onto the reflector, resulting in gas-desorption from the cavity as well as the inner funnel walls due to photon scattering, the gas being removed by the pumps in the system. This process goes on until the pressure is stabilized again at the baseline pressure of 0.1 nTorr. During this procedure the inner surfaces of the funnel are beam-scrubbed. The background can
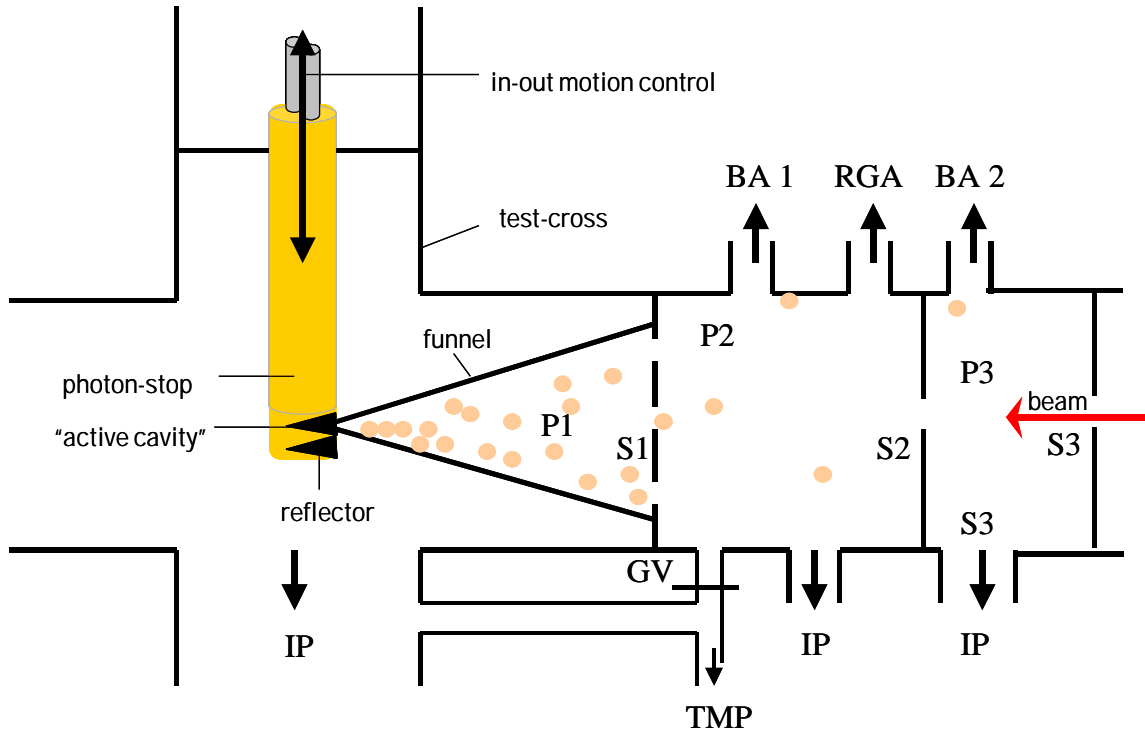
Figure 19: Sketch of photon stop vacuum test.

be further reduced by pre-treating the funnel (which should be made of steel) at high temperature (~900 C) in vacuum to reduce out-gassing. ANL has high temperature vacuum ovens. The other, so called "active" cavity, remains shielded by the funnel during the cleaning process.

After completion of the cleaning process the active cavity can be moved into the beam and the experiment can begin. In the case of multiple sample cavities this process can be repeated several times. We hope that this measure reduces the back-ground enough to make a measurement possible. An additional BA-gage mounted into one of the horizontal ports (not shown in Figure 17) to monitor the pressure in the cross-volume could be used to determine gas leakage through the small gap between the funnel and the absorber cavity.

5.2.3) Electron-emission

The photo-emission spectrum from the photon-stop is well known (consisting of a few fluorescence lines) and we believe that it would not be justified to invest in expensive photon-detectors to measure it. Instead, an integrated, indirect measure of the fluorescence yield can be obtained by measuring the e-emission from the surfaces hit by the fluorescent photons. The funnel can be isolated from ground with a ceramic ring at the flange, such that it can be negatively biased (-100 V) to allow measurement of electron emission from the funnel due to photons-emitted (or reflected) from the photon-stop. If, at the same time the photon-stop is biased positively (with V larger than the peak electron emission energy), secondary electron emission from the photon stop can be

suppressed. To measure the combined effect of photon and electron emission this experiment could be performed without electron emission suppression at the photon stop. The secondary electron emission from the photon stop can be measured separately by negatively biasing (-100 V) the photon-stop against ground and measuring the charge current caused by electron emission. This is a standard procedure that requires the photon stop to be electrically isolated from ground. As before, positive biasing of the funnel can help to reduce the effect of electron emission from the funnel on the measurement signal. The use of ceramic breakers is being explored in the design of the mechanical photon stop drive. Alternatively, a wire electrode could be introduced in the apparatus shown above (through the funnel wall at a point close to the photon stop). The electrode could form a loop in front of the sample, such that the photon beam will pass through the middle of it. More sophisticated devices, i.e. Faraday cups, ..etc, have not been considered yet. It could as well be envisaged to add a X-ray detector to the instrumentation arrays. AMPTEK offers an adequate detector (XR-100CR) for $ 3k. Details regarding the mounting (and shielding) of such a detector have not been addressed yet.

References:

[1]   P. Limon et al., "*Design Study for a Staged Very Large Hadron Collider*", Fermilab-TM-2149, June 2001.

[2]   M. Pivi, W.C. Turner, P. Bauer, P. Limon, "*Synchrotron Radiation and Beam Tube Vacuum in a Very Large Hadron Collider, Stage 1 and Stage 2*", Proceedings to the Particle Accelerator Conference 2001, Chicago, Sept. 2001

[3]   P. Bauer et al., "*Synchrotron Radiation Issues in the VLHC*", Proceedings to the Particle Accelerator Conference 2001, Chicago, Sept. 2001

[4]   P. Bauer, C. Darve, I. Terechkine, "*Synchrotron Radiation Issues in Future Hadron Colliders*", to be published in the proceedings of the 2001 Particle Physics conference at Snowmass

[5]   P. Bauer, C. Darve, I. Terechkine, "*Synchrotron Radiation Issues in Future Hadron Colliders*", Summary of the contributions to the T2 WG at the Snowmass 2001 conference, Fermilab, Technical Division note TD-01-061, August 2001

[6]   C. Darve et al: "*VLHC beam-screen cooling*", Fermilab, Technical Division Note TD-01-005, Feb. 2001

[7]   P. Bauer et al. "*Photon stop Engineering Design 1*", Fermilab, Technical Division note, TD-01-023, April 2001

[8]   N. Solyak, "*Photon Stop for the VLHC-2 – Impedance Calculations*", Fermilab, Technical Division Note TD-01-014

[9]   P. Bauer et al., "*Accelerator Physics and Technology Limitations in Stage II – type Very Large Hadron Colliders*", Summary of the contributions to the M4 WG at the Snowmass 2001 conference, Fermilab, Technical Division note, TD-01-062, October 2001

[10]   P. Bauer, S. Sharma, P. Limon, T. Peterson, N. Solyak, I. Terechkine, "*Photon Stop R&D Proposal*", Fermilab, Technical Division note, TD-01-030, June 2001

[11]   P. Bauer, "*Collection of Formulas for the Calculation of Synchrotron Radiation emitted by bending Magnets and Undulators*", Fermilab, Technical Division Note TD-02-020, 2002

[12]   W.C. Turner, "*Beam Tube Vacuum in Future Superconducting Proton Colliders*", SSCL Preprint-564, Oct. 1994

[13]   O. Groebner, "*The VLHC Vacuum System*", Proceedings of the 1997 Particle Accelerator Conference, Vancouver, Sept. 1997

[14]   P. Bauer, "*Review of SSC and LHC Beam Screen Vacuum Experiments*", Fermilab, Technical Division Note TD-02-013, April 2002

[15]   M. Pivi, W.C. Turner, "*Synchrotron Radiation Effect on Dynamical Vacuum with Localized Photon Stops in a VLHC Stage 2 Beam Screen Section*", unpublished draft, Jan 2002

[16]   R. Cimino, I.R. Collins, V. Baglin, "*VUV Photoemission Studies of Candidate LHC Vacuum Chamber Materials*", LHC Project Report 256, CERN, 1998

[17]   J.A. Bearden, "*X-ray Wavelengths*", in Review of Modern Physics, Jan. 1967, p. 86-99;

[18]   M.O. Krause, J. Phys. Chem. Ref. Data 8,307, 1979

[19]   Handbook of Chemistry and Physics, D.R. Lide, 78th edition, CRC Press, 1998

[20]   S. Eisebitt, T. Boeske, J. Rubensson, W. Eberhardt, "*Determination of absorption coefficients for concentrated samples by fluorescence detection*", Physical Review B, Vol. 47, 21, p. 14103, 1993

[21]   C. Foerster, C. Lanni, J.R. Noonan, R.A. Rosenberg, "*Photon Stimulated Desorption Measurements of an Extruded Aluminum Beam Chamber for the APS*", J.Vac.Science+Technol., A 14(3), p.1273, 1996